Journal of Geophysical Research: Space Physics

RESEARCH ARTICLE
10.1029/2018JA025690

A New Empirical Model of the Subauroral Polarization Stream

B. S. R. Kunduri[1], J. B. H. Baker[1,2], J. M. Ruohoniemi[1], N. Nishitani[2], K. Oksavik[1,3,4], P. J. Erickson[5], A. J. Coster[5], S. G. Shepherd[6], W. A. Bristow[7], and E. S. Miller[8]

[1]Center for Space Science and Engineering Research (Space@VT), Virginia Polytechnic Institute and State University, Blacksburg, VA, USA, [2]Institute for Space-Earth Environmental Research, Nagoya University, Nagoya, Japan, [3]Department of Physics and Technology, Birkeland Centre for Space Science, Bergen, Norway, [4]Arctic Geophysics, University Centre in Svalbard, University of Bergen, Bergen, Norway, [5]Atmospheric Sciences Group, MIT Haystack Observatory, Westford, MA, USA, [6]Thayer School of Engineering, Dartmouth College, Hanover, NH, USA, [7]Geophysical Institute, University of Alaska Fairbanks, Fairbanks, AK, USA, [8]The Johns Hopkins University Applied Physics Laboratory, Laurel, MD, USA

Abstract Regions of persistent westward directed flows are often observed equatorward of the auroral oval in the dusk-midnight sector. In general, the midnight narrow flows are termed as subauroral ion drifts and the duskside broader flows are termed subauroral polarization streams (SAPS). SAPS/subauroral ion drift electric fields play an important role in controlling the dynamics of the midlatitude ionosphere. In this paper we analyze longitudinally extended observations of SAPS measured by midlatitude Super Dual Auroral Radar Network (SuperDARN) radars under varied geomagnetic conditions. We find that SAPS speeds exhibit a strong dependence on geomagnetic activity, with flows exceeding 1,500 m/s during geomagnetic storms and dropping to 100 m/s during periods of geomagnetic quiet. Moreover, SAPS flows turn increasingly poleward when moving from the midnight sector toward dusk and this effect is more pronounced during disturbed geomagnetic conditions. The variations in SAPS speeds with magnetic local time (MLT) are also found to be strongly dependent on geomagnetic conditions. Specifically, SAPS speeds increase quasilinearly with MLT during disturbed geomagnetic conditions, whereas during relatively quiet geomagnetic conditions there is no discernible trend. This behavior suggests the possibility of different mechanisms influencing SAPS during geomagnetically quiet conditions. Average cross-SAPS potentials increase with geomagnetic activity and typically vary between 15 and 45 kV. Finally, a new empirical model of SAPS potentials has been developed parameterized by Asy-H index, MLT, and magnetic latitude.

Key Points:
- We present a new empirical model of SAPS potentials parameterized by Asy-H, MLT, and magnetic latitude
- SAPS speeds exhibit considerable differences during storm time and non-storm time conditions
- SAPS speeds increase quasilinearly with MLT during disturbed geomagnetic conditions; no trend is seen for quiet times

Correspondence to:
B. S. R. Kunduri,
bharatr@vt.edu

Citation:
Kunduri, B. S. R., Baker, J. B. H., Ruohoniemi, J. M., Nishitani, N., Oksavik, K., Erickson, P. J., et al. (2018). A new empirical model of the subauroral polarization stream. *Journal of Geophysical Research: Space Physics*, *123*, 7342–7357. https://doi.org/10.1029/2018JA025690

Received 17 MAY 2018
Accepted 9 AUG 2018
Accepted article online 21 AUG 2018
Published online 8 SEP 2018

1. Introduction

Regions of strong westward directed plasma flows equatorward of the auroral oval and predominantly in the dusk-midnight sector have been reported in the literature for more than 40 years. A number of terms such as polarization jets (PJ; Galperin et al., 1974), subauroral ion drift (Anderson et al., 1993, 2001; Spiro et al., 1979), subauroral electric fields (Karlsson et al., 1998), substorm-associated radar auroral surges (Freeman et al., 1992), and auroral westward flow channels (Parkinson et al., 2003) have been used to describe these subauroral electric fields. The term subauroral polarization streams (SAPS) was coined by Foster and Burke (2002) to encompass all these separately reported phenomena which exhibit a certain degree of similarity. They defined SAPS to be latitudinally broad regions (3–5° wide) of enhanced westward flows observed in the nightside subauroral region. Subauroral ion drifts (SAID)/PJ are latitudinally narrow (~ 1° wide) channels of intense westward flows often exceeding 1 km/s that are occasionally embedded within the SAPS channel (Foster & Burke, 2002; Oksavik et al., 2006). Furthermore, SAPS near substorm onsets comprise mesoscale, of order tens of kilometers in the ionosphere, quasiperiodic electromagnetic wave structures (SAPSWS; Mishin et al., 2003). In strong SAPSWS, the peak to peak variability is of the same order as the mean or even greater, resulting in SAPSWS being mistaken for multiple SAID channels.

The traditional paradigm of SAPS generation is as follows. During periods of enhanced geomagnetic activity, the ion Alfvén layer moves closer to Earth compared to the electron Alfvén layer due to the difference in energy spectra (Gussenhoven et al., 1987; Heinemann et al., 1989). Such a misalignment can set up strong radially outward polarization electric fields which map into the ionosphere along magnetic field lines in the poleward direction producing SAPS. However, Anderson et al. (1993) proposed that polarization electric fields generated due to simple misalignment in boundaries might not be the sole drivers of SAPS. Instead, the

misalignment in the boundaries causes a portion of the Region 2 field-aligned currents (FACs) to flow into a region of low conductance which hinders current closure resulting in the generation of the large poleward directed electric fields associated with SAPS (Anderson et al., 1993). The important role played by Region 2 FACs in driving SAPS/SAID was further supported by the observations presented in He et al., (2016, 2017, 2018). In addition, the enhanced electric fields lead to increased charge exchange rates and ion recombination resulting in further decrease in conductivity (Banks & Yasuhara, 1978; Schunk et al., 1976) producing a feedback effect that allows the electric fields to grow even more (Anderson et al., 1993, 2001). This form of ionospheric feedback is expected to play an important role in generating and sustaining SAPS since the fraction of Region 2 FACs flowing into the subauroral latitudes is generally small (Foster & Burke, 2002). Such ionospheric feedback generally depends on the duration of the storm and may become an important factor influencing SAPS/SAID flows, particularly during major geomagnetic storms. Recent studies have revealed new insights into SAPS driving mechanisms, challenging the traditional paradigm. Specifically, Mishin (2013) and Mishin et al. (2017) used magnetically conjugate observations to show that the broader SAPS flows and the narrow SAID channel may not be the same phenomenon and could also be driven by other mechanisms. Mishin et al. (2017) suggested that SAPS could also be generated when the upward current at the head of the two-loop substorm current wedge (SCW; e.g., Kepko et al., 2015) is partially closed by the downward current at subauroral latitudes via the Pedersen currents, setting up large poleward directed electric fields to maintain current closure in the low conductivity region. By contrast, they suggest that the narrow SAID channel is driven by the penetration of earthbound-ejected mesoscale hot plasma flows into the plasmasphere, suggesting that SAID can form even during pseudobreakups (without a SCW formation). Thus, the speed of a SAID channel (dependent on the energy of the intruding mesoscale hot plasma flow ions) can be great even during pseudobreakups and individual substorms with relatively small values of Dst/Asy-H index.

Significant increases in measurements from the coupled inner magnetosphere-ionosphere region during the last solar cycle have provided several new insights about SAPS. Specifically, the expansion of Super Dual Auroral Radar Network (SuperDARN) into the middle latitudes provided an excellent opportunity to make extended observations of SAPS during widely varying geomagnetic conditions (Clausen et al., 2012; Ebihara et al., 2009; Kataoka et al., 2007; Kunduri et al., 2012, 2017; Nagano et al., 2015; Oksavik et al., 2006). Recently, Kunduri et al. (2017) reported observations of SAPS even during geomagnetically quiet conditions and Nagano et al. (2015) showed that SAPS flows can have speeds as low as 150 m/s using measurements from the Hokkaido SuperDARN radar. Such observations of quiet time SAPS were further supported by measurements made by Van Allen Probes when $Kp \leq 2$ and $|Dst| \leq 20$ nT (Lejosne & Mozer, 2017). These studies show that SAPS are more persistent features of the subauroral ionosphere than previously realized and can be observed over a relatively wide range of geomagnetic conditions. Furthermore, Gallardo-Lacourt et al. (2017) and Lyons et al. (2015) showed strong correlations between SAPS enhancements (SAID) and auroral streamers. They suggested that auroral streamers can intensify SAPS by enhancing the pressure gradients in ring current, and flow bursts in the plasma sheet can reach the inner magnetosphere and strengthen SAPS flows. It is important to note that a relatively small value of Dst or Kp does not necessarily indicate weak SAPS/SAID flows, as they can develop during individual substorms and even pseudobreakups (Mishin, 2013; Mishin et al., 2017). A detailed discussion of the differences in the evolution of SAPS during intense storms and quiet time substorms was presented in He et al. (2017). During severe geomagnetic storms SAPS were typically observed in the dusk sector, earlier than 20 magnetic local time (MLT) and peaking around 18 MLT, whereas during quiet time substorms SAPS were observed later than 19 MLT, peaking around 21 MLT (He et al., 2017). Finally, previous studies (Goldstein et al., 2003, 2005; Lejosne et al., 2018) demonstrated that SAPS electric fields have a significant influence on the dynamics of the inner magnetosphere and discussed the necessity of developing an empirical model and a statistical characterization of SAPS representing a broader range of geomagnetic conditions (Goldstein et al., 2005).

Kunduri et al. (2017) developed an empirical model of SAPS occurrence probability and location using North American midlatitude SuperDARN radar data between 2011 and 2014. The current paper extends this analysis by examining the velocities (magnitude and direction), electric fields, and potentials associated with SAPS using the same database of events used in Kunduri et al. (2017). We find that SuperDARN observes SAPS with extremely low velocities during quiet geomagnetic conditions, and SAPS velocities and potentials exhibit a strong dependence on MLT and geomagnetic activity. We also present a new empirical model of SAPS potentials parameterized by Asy-H index representing a wide range of geomagnetic conditions.

Figure 1. Fields of view of the Northern Hemisphere Super Dual Auroral Radar Network radars highlighting the eight North American midlatitude radars used in this study.

2. Data Sets

2.1. SuperDARN High-Frequency Radars

The SuperDARN network is an international chain of radars covering polar, high, and midlatitudes in the Northern and Southern Hemispheres (Chisham et al., 2007; Greenwald et al., 1985, 1995) and played an important role in advancing our knowledge of ionospheric electrodynamics (Kim et al., 2013; Prikryl et al., 2013; Ruohoniemi & Baker, 1998; Shi et al., 2018). The ionospheric plasma drift observed by the North American chain of midlatitude SuperDARN high-frequency radars (de Larquier et al., 2011; Kunduri et al., 2012; Maimaiti et al., 2018) is the primary data set used in the current study. SuperDARN radars make measurements of coherent backscatter from decameter-scale field-aligned plasma irregularities. The Doppler shift of the backscattered signal is proportional to the line-of-sight component of the $\mathbf{E} \times \mathbf{B}$ plasma drift in the scattering region (Ruohoniemi et al., 1987). SuperDARN radars electronically steer their look directions, typically scanning through 16–24 beams in 1–2 min and covering an azimuth of $\sim$ 50°. Along each beam the returned scatter is sampled at 45-km steps called range gates. Typically there are 75 range gates providing a maximum range of ~3,500 km. Wallops Island was the first U.S. midlatitude radar which became operational in 2005. The construction of seven additional U.S. radars followed shortly and have been operational since the end of 2012. Figure 1 shows the fields of view of the SuperDARN radars in the Northern Hemisphere plotted in magnetic coordinates. In this study, we use data from the eight U.S. midlatitude radars (shaded in Figure 1) between January 2011 and December 2014 to identify and analyze SAPS events.

2.2. Other Data Sets

Particle precipitation data from the total energy detector instrument on board the National Oceanic and Atmospheric Administration Polar Orbiting Environment Satellites were used to determine the equatorward boundary of the auroral oval. A detailed description of the method employed to determine the equatorward auroral boundary was provided by Kunduri et al. (2017). Knowledge of the location of the auroral oval boundary is necessary to distinguish between high-latitude convection in the dusk sector and SAPS flows which

both tend to be westward. Another important data set used to parameterize SAPS flows is the Asy-H index (Iyemori et al., 1992) which is indicative of the strength of the partial ring current.

3. Observations

In this section, we discuss the methodology used to estimate velocities, electric fields, and potential drops across SAPS and examine the behavior of these parameters. We use the same list of SAPS events analyzed in Kunduri et al. (2017). Specifically, the line-of-sight velocity data from the eight U.S. midlatitude SuperDARN radars, between January 2011 and December 2014, were analyzed. Furthermore, to limit the selection to long-lived and large-scale SAPS events, only those flows located below the equatorward boundary of the auroral oval derived from Polar Orbiting Environment Satellites (Kunduri et al., 2017) and observed by at least four of the eight U.S. midlatitude radars were chosen.

3.1. SAPS Velocities

We begin by describing our method to determine the direction and magnitude of the SAPS velocities from the line-of-sight velocities (V_{LOS}) measured by midlatitude SuperDARN radars. The method involves applying L-shell fitting (Clausen et al., 2012; Kunduri et al., 2012; Ruohoniemi et al., 1989) to derive solutions of SAPS velocities (V_{SAPS}) on a specified geomagnetic grid. With the L-shell fitting technique we assume that SAPS have a constant direction and magnitude across some longitudinal span of radar measurements and thus expect a sinusoidal dependence of V_{LOS} on radar beam azimuth. By fitting a sinusoidal function to the variations in V_{LOS} with beam azimuth, we can determine the direction and magnitude of the two-dimensional SAPS flows.

In Figure 2 we demonstrate the methodology used to determine two-dimensional SAPS velocities. V_{LOS} data from the North American midlatitude SuperDARN radars during a scan at 0840 UT on 9 April 2011 are overlaid on a map marked in MLAT-MLT coordinates. The dashed circle is the equatorward boundary of the auroral oval, indicating that V_{LOS} below the circle belong to SAPS. In order to determine SAPS flow directions at different locations, we define a spatial grid and apply L-shell fitting at each cell of the grid. After some trial and error, we determined the best spatial scale of the grid to be 0.5° in magnetic latitude (roughly the size of a SuperDARN range gate) and 1 hr in MLT. This grid is overlaid on the map, and the center of each cell is marked with a cross (x). Two example sinusoidal fits to the V_{LOS} at the cells marked in red are shown in the insets. In the first inset, we show L-shell fits for a grid cell at midnight MLT encompassing V_{LOS} data spanning 1 hr in MLT from the Christmas Valley East and Christmas Valley West radars. We estimate V_{SAPS} in this cell to have a bearing of −81° and a magnitude of ∼1,200 m/s. In the second inset, a grid cell at 2 MLT with V_{LOS} predominantly from the Blackstone and Fort Hays East radars and spanning 2 hr in MLT is L-shell fitted and V_{SAPS} in this cell was estimated to have a bearing of −94° and a magnitude of ∼350 m/s. The uncertainty associated with L-shell fitting is expressed in terms of standard deviation error in estimated V_{SAPS}. For the event presented in Figure 2, the standard deviation errors in velocity magnitude are ∼40 and ∼20 m/s in the first (fitting at 0 MLT) and second (fitting at 2 MLT) insets, respectively.

To avoid contamination of the SAPS fitting results from other sources such as subauroral ionospheric scatter (Ribeiro et al., 2012) and to discard unreliable measurements, V_{LOS} flagged as ground scatter and those with magnitudes less than 50 m/s or backscatter power less than 3 dB are discarded. Furthermore, a few constraints are applied to improve the accuracy of the fitting and discard erroneous fits. Specifically, we apply L-shell fitting on V_{LOS} data spanning 1 hr in MLT and 0.5° in magnetic latitude (as marked by the grid) and retain the fit when (1) at least five unique azimuth values from V_{LOS} are present, (2) an azimuthal range covered by V_{LOS} is at least 40°, (3) V_{LOS} from at least one eastward and one westward looking radars are present, (4) the results indicate a predominantly westward flow direction (−90° ± 25°), and (5) Kolmogorov-Smirnov test validates the goodness of fits. If any of the above mentioned criteria fail, we repeat the process by expanding the longitudinal span of fitting in steps of 1 hr in MLT (e.g., L-shell fitting applied to the cell near 2 MLT shown in Figure 2 spans 2 hr in MLT). If the criteria fail even after expanding the MLT span to 3 hr, we assume the direction of SAPS flows in the cell to be the same as the nearest cell with a *good fit* and apply a cosine correction factor to determine the corresponding V_{SAPS} magnitude. The criteria discussed above ensure that only large-scale westward directed subauroral flows are used in the study, and any erroneous fits of V_{SAPS} are discarded. The use of Kolmogorov-Smirnov test (a nonparametric test) further reduces the error associated with V_{SAPS}. In the current study, we discard the values of V_{SAPS} where the Kolmogorov-Smirnov test yields a p value less than 10%.

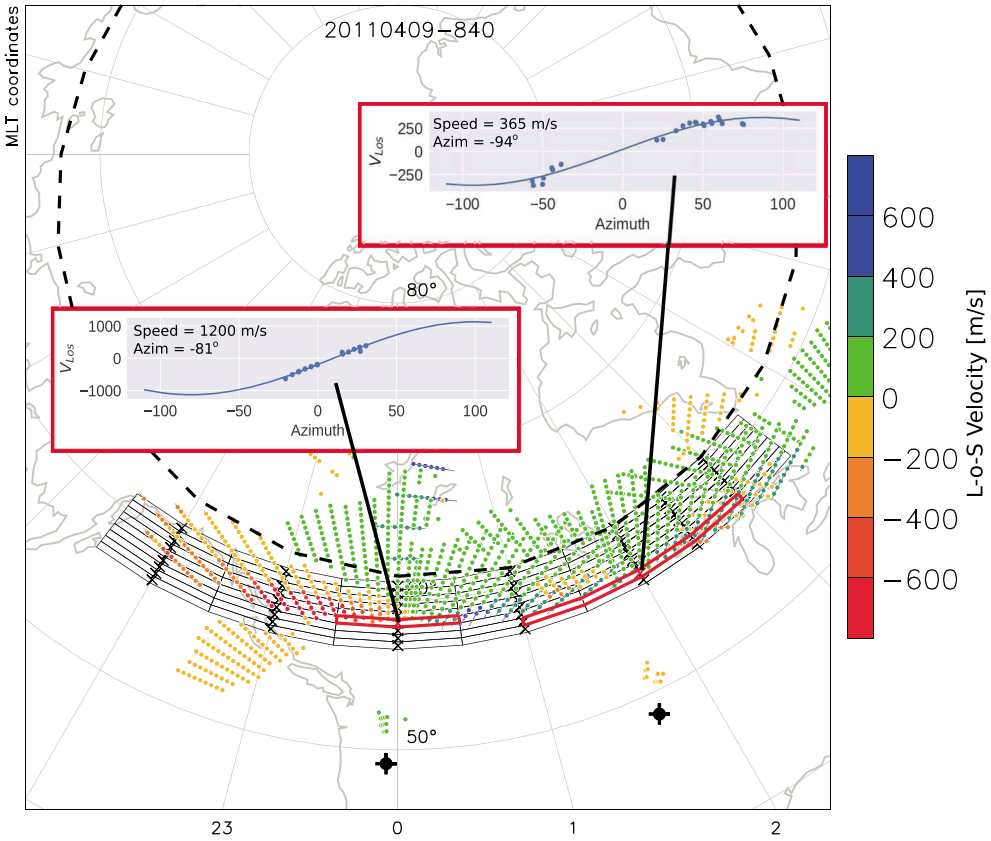

Figure 2. SuperDARN line-of-sight velocity observations during a SAPS event at 0840 UT on 9 April 2011 color coded according to the scale at right. Overlaid is the MLAT-MLT grid used for determining L-shell fitted 2-D SAPS velocities, and the dashed black circle represents the equatorward edge of the auroral oval determined using TED data from POES satellites. The insets show example sinusoidal fits of V_{LOS} versus radar azimuth at two MLAT-MLT locations. The longitudinal extent of the contributing V_{LOS} measurements is highlighted in red. See text for details. SuperDARN = Super Dual Auroral Radar Network; SAPS = subauroral polarization streams; MLAT = magnetic latitude; MLT = magnetic local time; TED = total energy detector; POES = Polar Orbiting Environment Satellites.

In Figure 3, we present V_{SAPS} estimated at different locations using the technique described above. Vectors beginning with filled circles indicate locations where L-shell fitting was successfully applied, whereas vectors beginning with open circles show locations where fitting criteria failed, so nearest neighbor information is partially used. Specifically, at such locations the direction of flows was assumed to be the same as the nearest good fit but the magnitude of the flows was determined by cosine fitting. During this particular event, SAPS speeds ranging between 300 and 1,200 m/s were observed. We examine the uncertainty associated with L-shell fitting before analyzing V_{SAPS} further. In Figure 4, we present a histogram of the standard deviation errors associated with V_{SAPS} magnitude (for all the events). It can be noted from the figure that ~ 70% of the uncertainty in fitting is lower than 25 m/s, and more than 90% values are lower than 50 m/s. Furthermore, a manual verification of fitting results showed that higher standard deviation errors were associated with higher V_{SAPS}. We can clearly observe from the figure that the uncertainties associated with L-shell fitting are significantly lower than the estimated magnitude of V_{SAPS}.

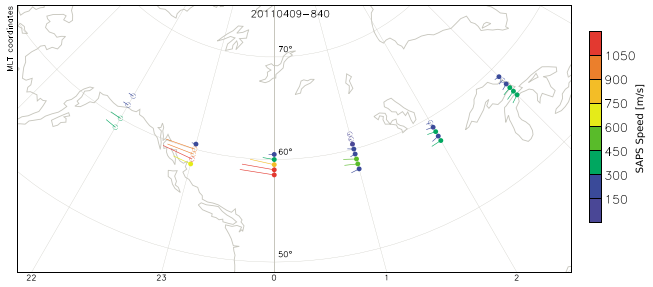

Figure 3. L-shell fitted SAPS velocity vectors for the V_{LOS} data presented in Figure 2. Vectors marked by filled circles indicate locations where fitting results satisfied all of the criteria described in the text, while vectors marked by open circles indicate locations where velocity directions were assumed to be the same as the nearest location marked by a filled circle. See text for details. MLT = magnetic local time.

3.2. Statistical Characterization of SAPS Velocities

We bin V_{SAPS} into four levels of geomagnetic activity based on Asy-H index, to determine the average behavior of SAPS in relation to the strength of the asymmetric ring current and substorm activity (Iyemori & Rao, 1996). The number of L-shell fitted vectors that were derived (using the

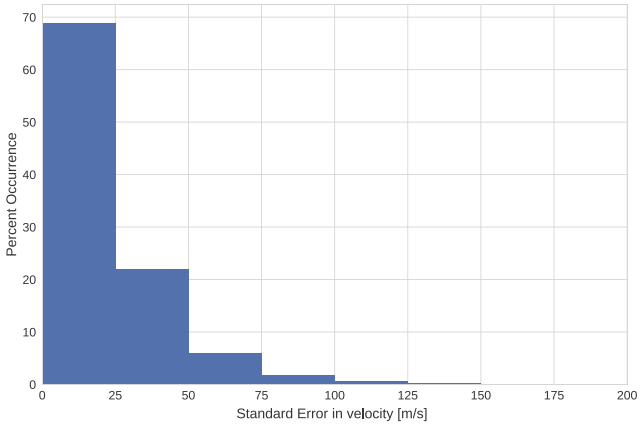

Figure 4. Histogram of standard deviation errors observed during L-shell fitting.

procedure described in the previous section) in each Asy-H index bin at different spatial locations is presented in Figure 5. While there are hundreds of vectors in each spatial and Asy-H index bin, we find that the number of samples in bins with lower geomagnetic activity (top row) is higher compared to bins indicating strong geomagnetic activity (bottom row). Such a difference in the number of samples is expected because the number of days with strong geomagnetic activity is much lower compared to geomagnetically quiet times. In Figure 6 we present median SAPS velocities in each Asy-H bin, scaled according to the color bar on the right and the size of the vector. A strong dependence of SAPS speeds on geomagnetic activity can be observed. Namely, when the Asy-H index is between 0 and 30 (top left panel) speeds ranging between 100 and 400 m/s are observed but when geomagnetic activity increases and Asy-H index exceeds 90 (bottom right panel) SAPS speeds range between 400 and 1,200 m/s. Furthermore, it can be noted that the direction of the flow turns increasingly poleward toward dusk as the geomagnetic activity increases. For example, when Asy-H index is between 60 and 90 (bottom left panel) SAPS speed increases from ~300 m/s at 1 MLT to ~1,000 m/s as we move toward 17 MLT (dusk). These features will be analyzed further in subsequent sections.

Figure 7 presents box plots of SAPS speeds versus MLT for each color-coded Asy-H index bin. Each box presents the quartiles (minimum, first quartile, median, third quartile, and maximum) of SAPS speeds observed at different Asy-H index bins and MLTs. Speeds beyond ±1.5× (interquartile range) are discarded as outliers. Clearly, SAPS speeds exhibit a wide degree of variability. When the geomagnetic conditions are disturbed SAPS speeds exceeding 1,500 m/s are observed, whereas during quiet geomagnetic conditions SAPS speeds as low as ~100 m/s are observed. Moreover, similar to the trend observed in Figure 6, two important features are observed: first, the pronounced increase in SAPS speeds with Asy-H bin at each MLT and second, the quasilinear increase in SAPS speeds with MLT when Asy-H index exceeds 60. These features will be discussed further and compared with results from previous studies in subsequent sections.

We now turn to analyzing the direction of SAPS flows. In Figure 8, we present median SAPS azimuths versus MLT for four Asy-H index bins with the vertical bars indicating standard deviations in azimuth. In this format, −90° is perfectly westward and increasing azimuths are indicative of poleward turning flows. For example,

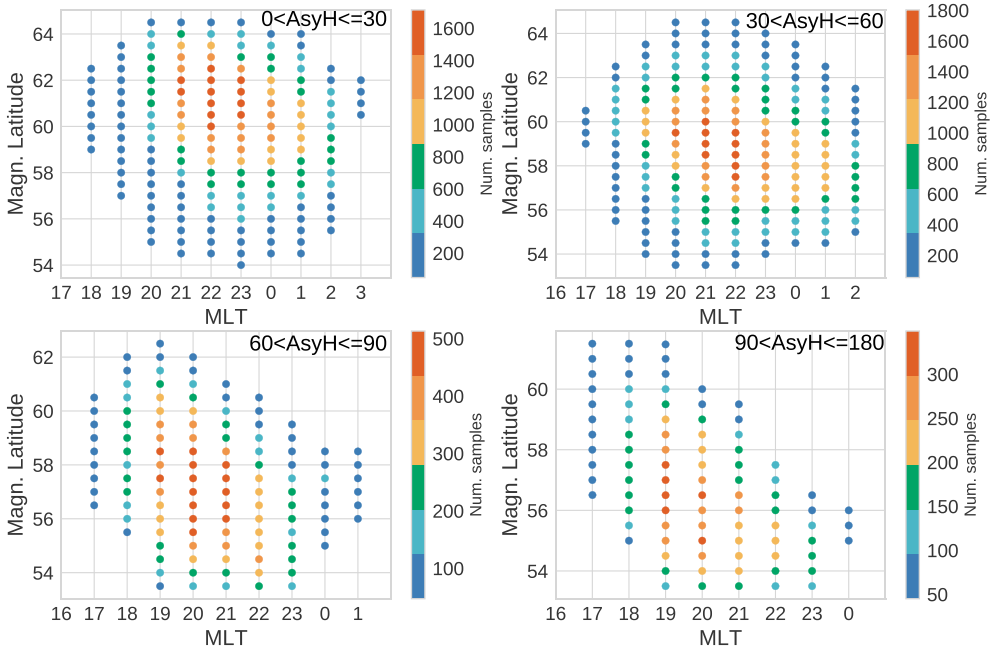

Figure 5. MLAT-MLT maps showing the number of L-shell fitted vectors calculated for four different Asy-H index bins. MLAT = magnetic latitude; MLT = magnetic local time.

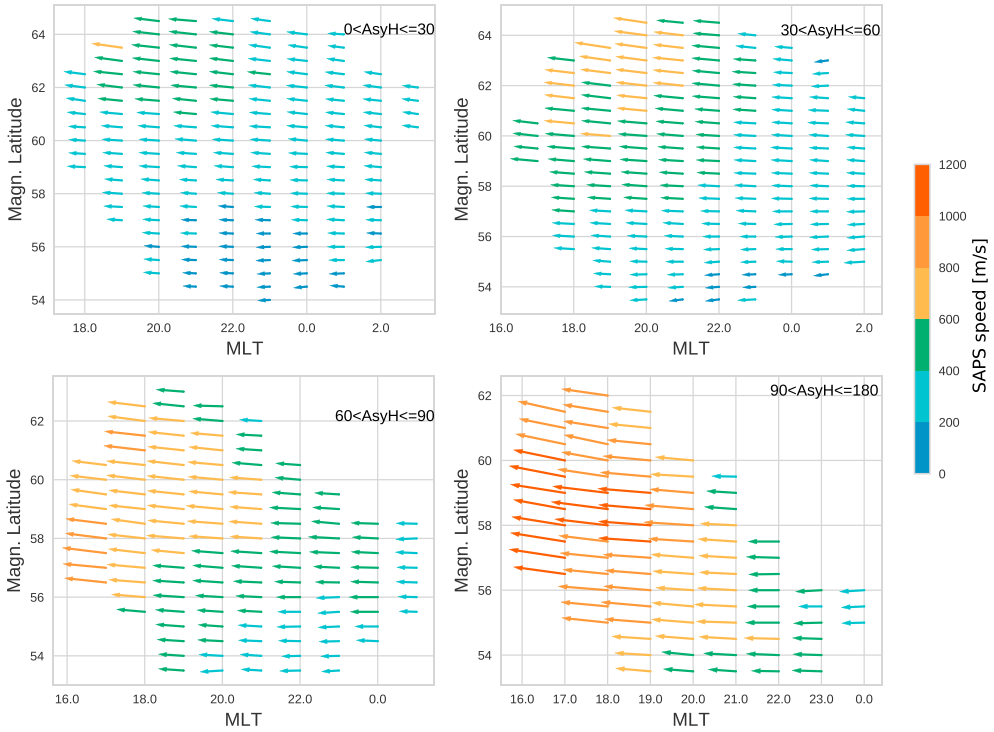

Figure 6. MLAT-MLT maps of median SAPS velocities for four different Asy-H index bins color coded according to the scale at right. MLAT = magnetic latitude; MLT = magnetic local time; SAPS = subauroral polarization streams.

an azimuth of −80° suggests that the flows are 10° poleward of the westward direction. A linear fit of SAPS azimuth with MLT is overlaid (solid lines), and the linear regression function is provided at the bottom left (ΔMLT_{00} indicates the MLT separation from midnight, which is MLT-24, if MLT > 12, or MLT otherwise). SAPS azimuths typically vary between −100° and −80° and turn increasingly poleward as we move toward the dusk sector. Furthermore, the rate at which flows turn poleward (indicated by the slope of the linear fit) is more pronounced during disturbed geomagnetic conditions. For example, when Asy-H index is between 30 and 60 (top right panel) the slope of the linear fit is 1°/MLT, whereas for the highest disturbance level (bottom right

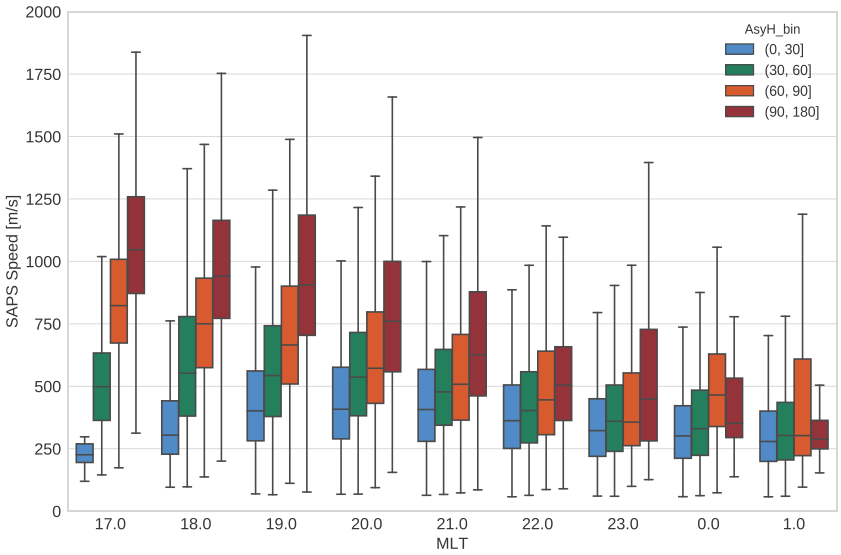

Figure 7. Box plots of SAPS speed versus MLT for four different color-coded Asy-H index bins versus MLT. SAPS = subauroral polarization streams; MLT = magnetic local time.

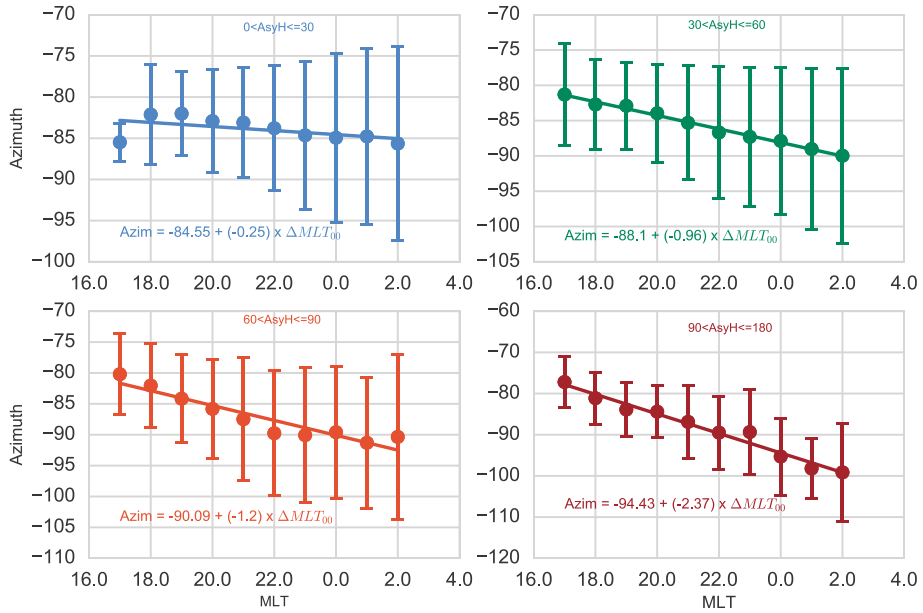

Figure 8. SAPS azimuth versus MLT with overplotted line of best fit for the four different Asy-H bins. Vertical bars indicate standard deviations. SAPS = subauroral polarization streams; MLT = magnetic local time.

panel) the slope of the fit increases to 2°/MLT. We will discuss the MLT dependence of SAPS azimuth further in the next section.

In Figure 9, we present the probability distributions of SAPS speeds at a specific Sun-fixed geomagnetic location (59° MLAT and 20 MLT) for the four Asy-H index bins, to analyze the variability observed in SAPS speeds. A few trends emerge. First, the most likely speed increases with geomagnetic activity (at the same geomagnetic

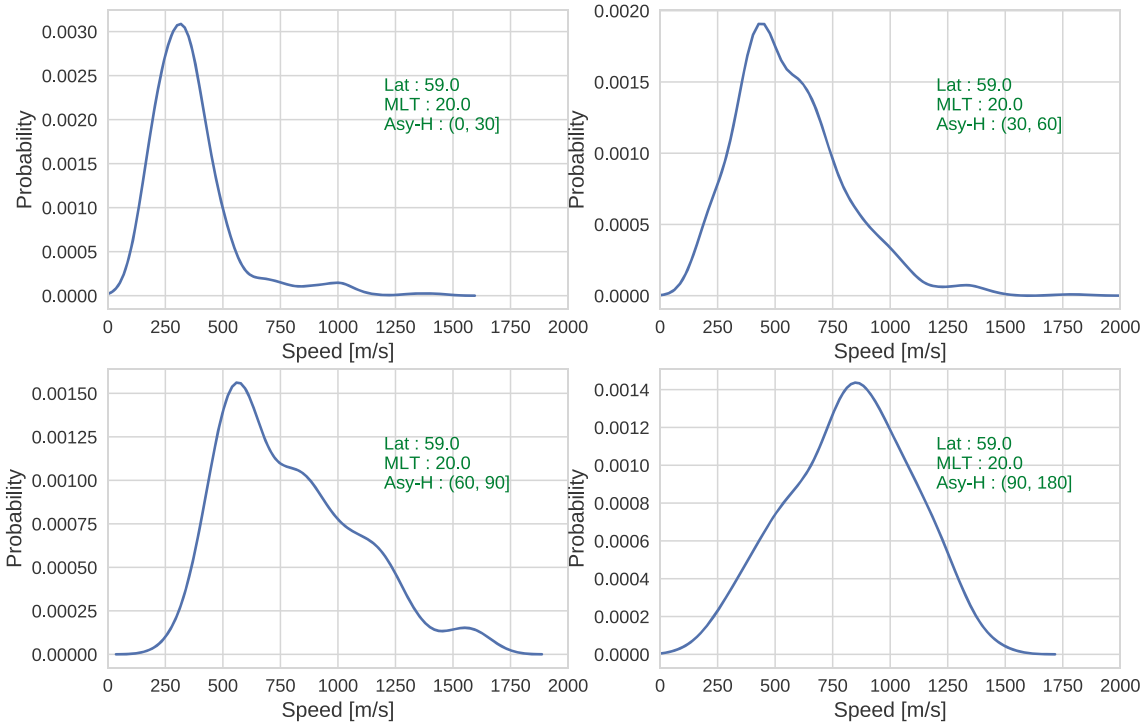

Figure 9. Probability distributions of SAPS speed at 59° MLAT and 20 MLT for the four Asy-H index bins. SAPS = subauroral polarization streams; MLT = magnetic local time.

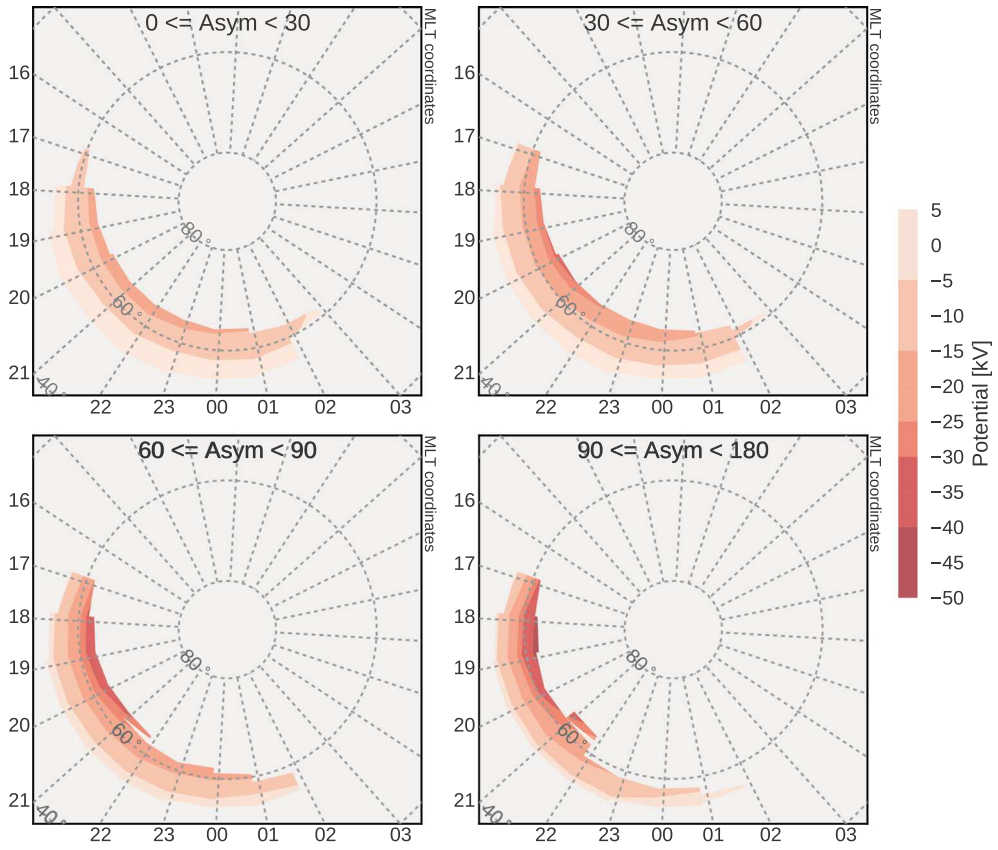

Figure 10. MLAT-MLT maps of SAPS electrostatic potential for the four Asy-H index bins.

location) and second, the spread in speeds is larger at higher geomagnetic disturbance levels. For example, when Asy-H index is less than 30 (top left panel), the most likely speeds are close to 300 m/s and the spread of the distribution is quite low with more than 80% of the speeds between 200 and 500 m/s, whereas for the highest disturbance level (bottom left panel) the most likely speed increases to $\sim$ 800 m/s and due to the increase in the spread of the distribution, there still is ~40% chance of observing velocities lower than 500 m/s. We will further explore this variability in SAPS flow speeds in later sections.

3.3. SAPS Potentials

The electrostatic potential patterns associated with SAPS (Φ_{SAPS}) play an important role in determining the dynamics of the inner magnetosphere (Foster & Vo, 2002; Goldstein et al., 2003, 2005). In this section we derive Φ_{SAPS} by poleward integration of SAPS electric fields and analyze its dependence on geomagnetic activity. We estimate SAPS electric fields from V_{SAPS} assuming $\mathbf{E} \times \mathbf{B}$ drift and using International Geomagnetic Reference Field-12 coefficients (Thébault et al., 2015) to estimate Earth's magnetic field in the SAPS region. A detailed description of the method is provided in Foster et al. (1982) and Foster and Vo (2002). Figure 10 presents MLAT-MLT maps of Φ_{SAPS} for the four Asy-H index bins. Poleward directed electric fields associated with SAPS imply a negative gradient in the electrostatic potential in the poleward direction. Similar to the trends observed in V_{SAPS}, the magnitude of Φ_{SAPS} increases with geomagnetic activity and is typically higher toward dusk. For example, when the geomagnetic activity is low and Asy-H index is between 0 and 30 (top left panel), Φ_{SAPS} varies between −5 and −15 kV, but when Asy-H index exceeds 90 (bottom right panel), Φ_{SAPS} ranges between −15 and −45 kV. In the next sections this behavior of Φ_{SAPS} is encoded into an empirical model and analyzed further.

3.4. Modeling SAPS Potentials

In the previous sections we found SAPS to exhibit a strong dependence on three parameters, namely, geomagnetic activity (indicated by Asy-H index), MLT, and MLAT. We will therefore model Φ_{SAPS} as a negative potential drop which is a function of these three parameters, similar to the approach taken by Goldstein et al. (2005). In particular, the following properties of Φ_{SAPS} (refer Figure 10) are encoded into the model: (1) peak value of Φ_{SAPS} increases with Asy-H index, (2) for a given Asy-H index bin, Φ_{SAPS} is strongest toward dusk and systematically decreases toward the midnight sector, and finally, (3) for a given Asy-H index bin and at a given

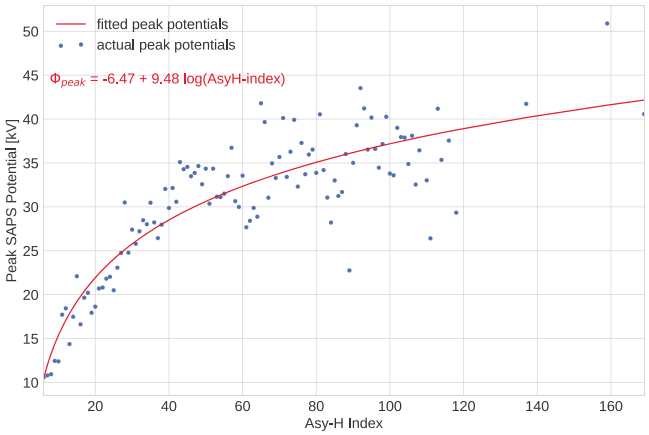

Figure 11. Peak SAPS potentials versus Asy-H index. The red curve represents a logarithmic fit to the data, and parameters of the fit are shown at upper left. SAPS = subauroral polarization streams.

MLT, Φ_{SAPS} increases in magnitude with MLAT. The assumed functional form of Φ_{SAPS} is therefore

$$\Phi_{SAPS}(\text{AsyH,MLT,MLAT}) = -\Phi_{PEAK}(\text{AsyH})\times F(\text{MLT, AsyH})\times G(\text{MLT,MLAT,AsyH}) \quad (1)$$

where Φ_{PEAK}(AsyH) quantifies the dependence of Φ_{SAPS} on Asy-H index, *F(MLT, AsyH)* quantifies the MLT dependence of Φ_{SAPS}, and *G(MLT,MLAT,AsyH)* represents the latitudinal variations of Φ_{SAPS}. Each of the three components is further described below.

3.4.1. Modeling Geomagnetic Activity Dependence of Φ_{SAPS}

In order to examine the dependence of Φ_{SAPS} on Asy-H index, in Figure 11 we plot median values of peak Φ_{SAPS} (referred to as Φ_{PEAK} from here on) versus Asy-H index. It can clearly be seen that Φ_{PEAK} exhibits a strong nonlinear dependence on geomagnetic activity. We model this behavior as a logarithmic function (indicated by the red curve) as follows:

$$\Phi_{PEAK} = A^{\Phi} + B^{\Phi}\log(\text{AsyH}) \quad (2)$$

where the parameters of the fit (A^{Φ}, B^{Φ}) are shown at the top left.

3.4.2. Modeling MLT Dependence of Φ_{SAPS}

From previous sections we note two important features characterizing the relation between Φ_{SAPS} and MLT: first, the peak location of Φ_{SAPS} moves further duskward with increasing geomagnetic activity and second, for a given Asy-H index bin Φ_{SAPS} decreases moving from dusk toward the midnight sector. Following the Goldstein et al. (2005) approach, we encode this behavior as a second-order Fourier series:

$$F = \sum_{n=1}^{2}\left[A_n\cos(n\phi) + B_n\sin(n\phi)\right] \quad (3)$$

where

$$\phi = (\pi/12)\times \text{mlt} + \phi_0 \quad (4a)$$

$$\phi = (\pi/12)\times \text{mlt} + \phi_0 \quad (4b)$$

$$A_n = X_n^A + Y_n^A \times \text{AsyH} \quad (4c)$$

$$B_n = X_n^B + Y_n^B \times \text{AsyH} \quad (4d)$$

Figure 12 demonstrates the fitting results used to determine equations (3) to (4d). Normalized SAPS potentials versus Asy-H index for four different Asy-H index bins are shown. The red curves are the Fourier series fits to the data (equation (3). It can be seen that the model captures the two features discussed above. For example, when Asy-H is between 30 and 60 (top right), the peak location of Φ_{SAPS} is between 21 and 22 MLT but when Asy-H exceeds 90 (bottom right), the peak location of Φ_{SAPS} moves duskward between 18 and 19 MLT. Furthermore, for a given Asy-H index bin Φ_{SAPS} systematically decreases from dusk toward midnight.

3.4.3. Modeling MLAT Dependence of Φ_{SAPS}

Figure 13 shows functional fits of the normalized MLAT versus normalized Φ_{SAPS} when Asy-H index is between 60 and 90 at 18 MLT (left panel) and 23 MLT (right panel). The actual values of MLAT (top axes) and Φ_{SAPS} magnitude (right axes) are also shown for reference. The blue dots are actual data points, and the red curve represents a second degree polynomial fit to the data specified by the following:

$$G = A^G + B^G \times \text{MLAT}_{\text{NORM}} + C^G \times \text{MLAT}^2_{\text{NORM}} \quad (5)$$

where

$$A^G = X_A^G + Y_A^G \times \text{AsyH} + Z_A^G \times \Delta\text{MLT}_{00} \quad (6a)$$

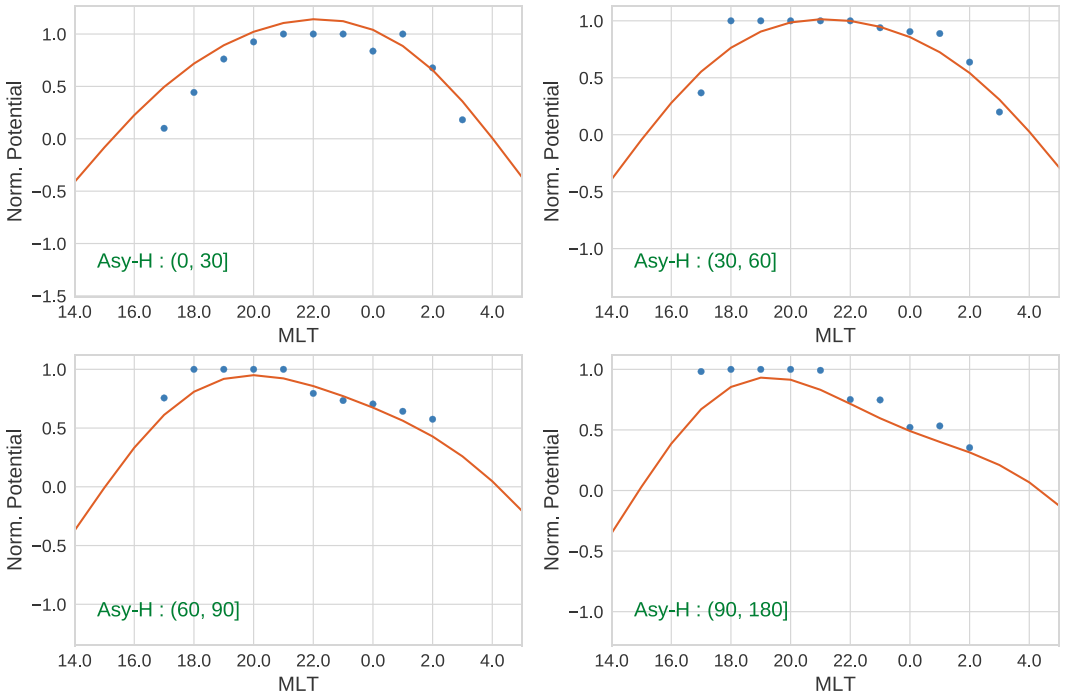

Figure 12. Normalized SAPS potentials versus MLT for four different Asy-H index bins. The red curves represent second-order Fourier series fits to the data. SAPS = subauroral polarization streams; MLT = magnetic local time.

$$B^G = X_B^G + Y_B^G \times \mathrm{AsyH} + Z_B^G \times \Delta\mathrm{MLT}_{00} \tag{6b}$$

$$C^G = X_C^G + Y_C^G \times \mathrm{AsyH} + Z_C^G \times \Delta\mathrm{MLT}_{00} \tag{6c}$$

$$\Delta\mathrm{MLT}_{00} = \begin{cases} \mathrm{MLT} & \text{if MLT} < 12 \\ \mathrm{MLT} - 24 & \text{otherwise} \end{cases} \tag{6d}$$

From Figure 13 we can observe that Φ_{SAPS} increases with MLAT. For example, at 18 MLT (left) Φ_{SAPS} increased from ~2.5 kV at 54° MLAT to ~40 kV at 63° MLAT and at 20 MLT Φ_{SAPS} varied between ~2 and ~30 kV for MLAT ranging between 53° and 64°. We find that Φ_{SAPS} exhibits a similar behavior at different Asy-H index bins and MLTs (not shown), and a polynomial fit captures this behavior. For the purpose of fitting the data, we normalized MLAT and Φ_{SAPS} to values between 0 and 1 as shown in the figure.

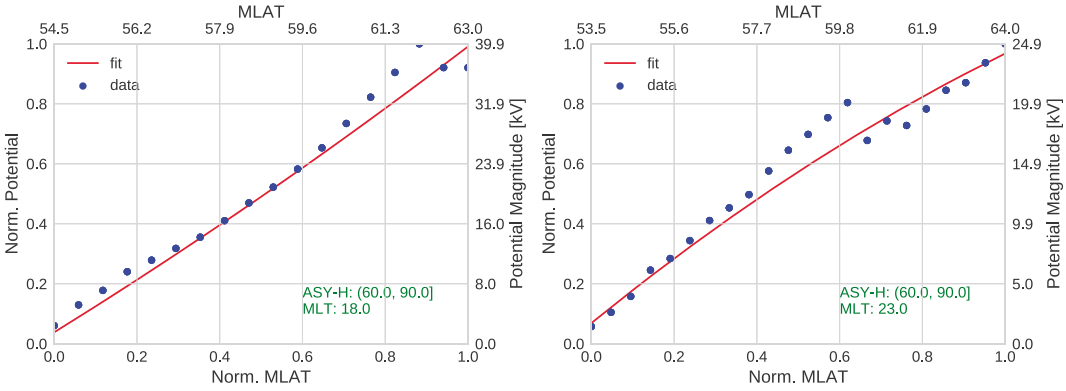

Figure 13. Normalized SAPS potentials versus normalized MLAT at 18 MLT (left) and 20 MLT (right). Actual MLAT values are also marked on the plots. The red curves represent polynomial fits to the data. See text for details. SAPS = subauroral polarization streams; MLAT = magnetic latitude; MLT = magnetic local time.

Table 1
Parameters and Standard Deviation Errors of SAPS Potential Fitting Presented in Section 3.4

Parameter	Value	Error
A^{Φ}	−6.47	1.92
B^{Φ}	9.48	0.48
ϕ_0	−3.4801	1.12
X_1^A	−0.7353	0.115
Y_1^A	0.0027	0.0003
X_1^B	1.0262	0.52
Y_1^B	−0.0023	0.0003
X_2^A	0.091	0.023
Y_2^A	−0.0023	0.0007
X_2^B	0.1036	0.023
Y_2^B	0.0016	0.0003
X_A^G	0.04777	0.011
Y_A^G	0.00053	0.00008
Z_A^G	0.00623	0.0031
X_B^G	0.85795	0.065
Y_B^G	0.006883	0.00072
Z_B^G	0.061588	0.016
X_C^G	0.07129	0.0061
Y_C^G	−0.00795	0.0006
Z_C^G	−0.077798	0.011

Note. SAPS = subauroral polarization streams.

Every parameter of the Φ_{SAPS} fit specified by equations (1) to (5) and the corresponding standard deviation errors are listed in Table 1. The MLT, MLAT inputs for the model of Φ_{SAPS} can be estimated using the SAPS location model presented in Kunduri et al. (2017). It should be noted that the selection criteria and the L-shell fitting technique used in this study limit our analysis to large-scale SAPS events observed across multiple radars and likely discard latitudinally narrow features such as SAID. A detailed analysis of SAID and SAPS formation mechanisms and their differences (e.g., Mishin, 2013; Mishin et al., 2017) is beyond the scope of the current study and will be explored in the future. Together, the SAPS location model of Kunduri et al. (2017) and the current model for Φ_{SAPS} can be used to estimate SAPS location and Φ_{SAPS} based on the Asy-H index and Dst values.

3.4.4. Model Data Comparison

In this section, the utility of the SAPS model is demonstrated by comparing model estimates of SAPS potentials with actual observations of SAPS flows during an event (not used for training the model) on 2 February 2015. *Dst* index during this event dropped to ∼ −30 and *Asy-H* index exceeded 55. Figure 14 shows the resulting model-data comparisons during the event. Panels (a) and (b) of the figure show V_{LOS} and V_{SAPS} (in midlatitude SuperDARN) during the event, respectively. It can be clearly noted that V_{SAPS} increases toward dusk and exceeds 1 km/s near 18 MLT, consistent with the average pattern of SAPS presented in Figures 6 and 7. In Figure 14c we present Φ_{SAPS} derived from actual observations, whereas in Figure 14d we present the model predictions of Φ_{SAPS}. The model predicts SAPS to be centered ∼ 60° MLAT spanning between 18 and 1 MLT, in agreement with the observations. The shorter MLT span of SAPS flows (between 19 and 0 MLT) in actual observations could be attributed to the lack of measurements in a few radars (e.g., WAL). The model predicts a peak Φ_{SAPS} of ∼30 kV near 21 MLT, in agreement with actual observations reaching 25 kV in the same MLT sector. Some differences between the model predictions and observations are expected because of the variability observed in SAPS speeds (shown in Figures 7 and 9). In summary, the model shows good agreement with actual measurements during the test event, capturing several important features of SAPS flows and will be useful in understanding the average behavior of SAPS under different geomagnetic conditions.

4. Discussion

In the previous sections, we have developed a methodology to derive SAPS velocities, electric fields, and potentials which were then grouped into different geomagnetic activity levels and their average characteristics analyzed. It was observed that V_{SAPS} and Φ_{SAPS} exhibit a strong dependence on geomagnetic activity and MLT. Also, the average statistical characteristics of Φ_{SAPS} have been coded into an empirical model based on Asy-H index. In this section, we discuss the behavior of V_{SAPS} and Φ_{SAPS} in more detail and compare the results with previous studies.

We begin by interpreting the behavior of SAPS azimuths and their dependence on geomagnetic activity and MLT. Previous statistical studies based on radar observations have generally assumed that SAPS flows were perfectly westward and applied a cosine correction factor to estimate flow speeds (Erickson et al., 2011; Foster & Vo, 2002; Kunduri et al., 2017). In this study we apply L-shell fitting on a statistical scale to estimate the direction of SAPS at different MLTs for the four Asy-H index bins (Figure 8). We find that SAPS flows turn increasingly poleward from a roughly westward orientation (∼ −90°) near midnight, for a broad range of geomagnetic activity. The rate of this duskward turning (indicated by the slope of the fit) is more pronounced at higher geomagnetic activity levels. These observations are consistent with the idea that SAPS flows eventually merge with high-latitude convection in the dusk-noon sector. Furthermore, a strong poleward component in SAPS flows especially during disturbed geomagnetic conditions supports previous studies associating SAPS with storm-enhanced density plumes (Foster et al., 2007; Zou et al., 2014).

Turning now to SAPS speeds, we can observe from Figures 6 and 7 that SAPS speeds increase with Asy-H index. This behavior can be attributed to Asy-H index being indicative of the strength of asymmetric ring current and an increase in the asymmetric ring current driving stronger Region 2 FACs resulting in an increase in SAPS speeds. Another noteworthy point from Figures 6 and 7 is that SAPS speeds can drop to ∼100–150 m/s (corresponding to electric fields lower than 5 mV/m), when the *Asy-H* index drops below 30. These results are comparable to the 150- to 200-m/s velocity range reported in Nagano et al. (2015) and almost an order of magnitude lower than the electric fields (≥ 50 mV/m) required to generate frictional heating in the trough

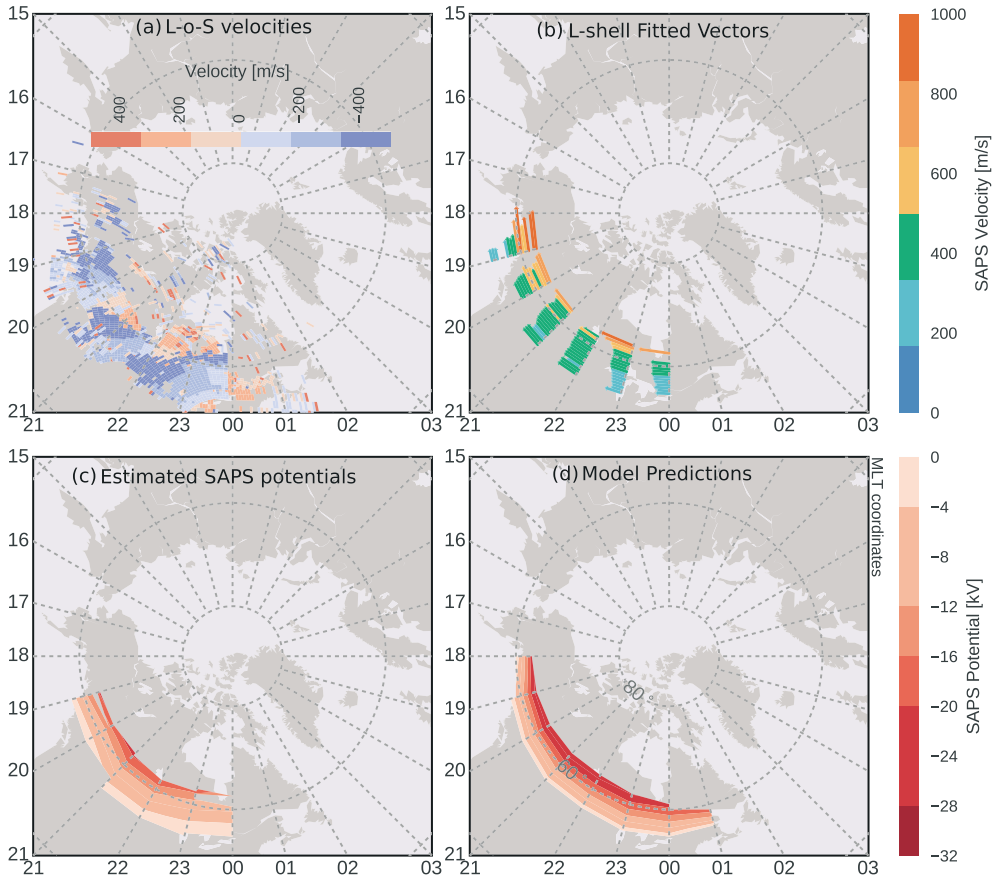

Figure 14. Model data comparison for a SAPS event observed by the midlatitude SuperDARN radars, on 2 February 2015. Panels (a) and (b) present actual line-of-sight velocities and L-shell fitted vectors from a SAPS channel, observed by the U.S. midlatitude SuperDARN radars, respectively. Panel (c) presents SAPS potentials derived from actual observations, and panel (d) presents SAPS potentials predicted by the model. SuperDARN = Super Dual Auroral Radar Network; SAPS = subauroral polarization streams; MLT = magnetic local time.

and produce ionospheric feedback (Schunk et al., 1976), an important mechanism enhancing and sustaining SAPS. Similarly, differences in the distributions of SAPS speeds at different geomagnetic activity levels can be observed in Figure 9. For the lowest disturbance level (top left panel), typical SAPS speeds are observed to vary between 200 and 500 m/s and as expected, SAPS speeds increase with geomagnetic activity level and typically exceeding 800 m/s when *Asy-H* index reaches 90. However, it is interesting to note that the spread in SAPS speed increased with geomagnetic activity. This behavior shows the dynamic nature of SAPS flows and how individual SAPS events can deviate significantly from the average or expected behavior. Possible influences responsible for this variability include ionospheric conductivity, strength of ring current, IMF, and substorm activity.

The overall behavior of SAPS speeds presented here is similar to the results from previous statistical studies such as Erickson et al. (2011) and Foster and Vo (2002). Although a direct one-to-one comparison is not possible with these studies since they use different geomagnetic indices (Kp and Dst, respectively) to characterize SAPS, a qualitative comparison based on geomagnetic activity level shows that the observations are in good agreement. For example, during highly disturbed geomagnetic conditions when *Asy-H* exceeds 60 nT, *Dst* drops below −50 nT and $Kp \geq 6$; SAPS speeds exceeding 1 km/s are reported near dusk in all the studies, whereas during relatively quiet times ($Asy\text{-}H < 60$, $Dst > -50$, and $Kp \leq 4$) median SAPS speeds between 250 and 500 m/s are observed. While the average behavior shows SAPS speeds increase with geomagnetic activity, a closer examination reveals a more complex behavior. In particular, the box plots and the probability distributions of SAPS speeds shown in Figures 7 and 9, respectively, suggest that SAPS flows in some cases can reach very high speeds (~1 km/s) even when Asy-H index is not very large. For example, Figure 7 shows that maximum SAPS speeds can reach up to 1 km/s even when $Asy\text{-}H < 60$. A similar behavior is observed in

Figure 9 which shows that a fraction of SAPS flows reach high speeds (exceeding 750 m/s) during relatively quiet conditions. These observations support the idea that SAPS and SAID may not be the same phenomenon and that strong SAID flows can be observed during individual substorms and pseudobreakups with relatively small values of Asy-H inde (Mishin, 2013, 2016; Mishin et al., 2017).

A majority of previous studies find that SAPS exhibit a strong dependence on MLT (Erickson et al., 2011;Foster & Vo, 2002; He et al., 2018, 2017). Recent results presented in He et al. (2017) suggest that SAPS occurrence maximized around 18 MLT during severe geomagnetic storms and near 21 MLT during quiet time substorms. Our results presented in Figure 7 indicate a similar trend and are in agreement with He et al. (2017) in that we find that SAPS flows are strongest near the dusk sector (∼18 MLT) during disturbed geomagnetic conditions, whereas during relatively quiet conditions SAPS speeds maximize between 19 and 21 MLT. However, there has been some disagreement on the dependence of SAPS speeds on MLT. Clausen et al. (2012) found an exponential dependence of SAPS speeds on MLT by analyzing a single event, whereas a statistical analysis by Erickson et al. (2011) showed a linear trend. In the current study, we find a linear increase in SAPS speeds toward dusk, during disturbed geomagnetic conditions (*Asy-H* index > 60), consistent with the intensification and duskward rotation of the asymmetric ring current during geomagnetic storms (Liemohn et al., 2001; Toffoletto et al., 2003; Tsyganenko, 2002a, 2002b). However, this linear trend is not as pronounced for the lower geomagnetic activity levels (*Asy-H* index < 60), indicating that the asymmetric ring current may not be the primary driver of SAPS during nonstorm conditions. Indeed, the various differences between disturbed time and quiet time SAPS presented in this paper support new theories suggesting alternative mechanisms for driving SAPS such as the inherent current closure in the SCW (Mishin et al., 2017).

Turning now to Φ_{SAPS}, we find the magnitude of Φ_{SAPS} to typically vary between 5 and 50 kV depending on geomagnetic conditions and MLT, as shown in Figure 10. Similar to the trends observed in SAPS speeds, Φ_{SAPS} increases with geomagnetic activity and toward dusk. Φ_{PEAK} increased logarithmically with Asy-H index and typically exceeded 15 kV. These values of Φ_{PEAK} suggest that SAPS have a significant influence on ionospheric electrodynamics even during nonstorm conditions. A statistical characterization of SAPS potentials was previously presented in Foster and Vo (2002) for $Kp \geq 4$ conditions. They show that when $Kp > 6$, potential drops from 15 to 30 kV are observed and when *Kp* exceeds 7, they report SAPS potential drops greater than 50 kV in magnitude. These values show an overall agreement with the estimates presented in the current study, in a qualitative sense. A magnetospheric model of SAPS potential was developed by Goldstein et al., (2003, 2005) for $Kp \geq 4$ conditions, based on average SAPS characteristics presented in Foster and Vo (2002). It was demonstrated that including the Goldstein et al. (2005) model to incorporate the effects of SAPS electric fields on the dynamics of inner magnetosphere improved the performance of simulations predicting the location and shape of plasmaspheric plumes. However, parameterizing the model by Kp index with a 3-hr cadence was considered to be a serious weakness and it was suggested that a better characterization of SAPS was needed (Goldstein et al., 2005). We believe that our model of Φ_{SAPS} based on Asy-H index along with the SAPS location model developed by Kunduri et al. (2017) fits this need because it covers a wider range of geomagnetic activity and therefore addresses the concerns raised by (Goldstein et al., 2005). Looking forward, our empirical Φ_{SAPS} model could be particularly useful validating theoretical simulations of SAPS and thereby contribute to an improved understanding of the coupled inner magnetosphere-ionosphere dynamics.

5. Conclusions

This paper presents a statistical analysis of the speed, flow direction, and potential drops associated with large-scale SAPS events observed by the U.S. midlatitude SuperDARN radars. We developed a technique based on L-shell fitting to estimate SAPS flow magnitude and direction with good statistics. We find that SAPS speeds exhibit a high degree of variability and show a strong correlation with geomagnetic activity. During geomagnetic quiet SAPS speeds as low as ∼100 m/s were observed but increased in magnitude with disturbance level, often exceeding 1,500 m/s during geomagnetic storms. Furthermore, SAPS flows showed a strong dependence on MLT with the flows turning increasingly poleward and the speeds increasing toward dusk. We developed maps of average SAPS potentials binned by Asy-H index and found peak SAPS potentials increase with geomagnetic activity and typically vary between 15 and 45 kV, suggestive of their significant influence on ionospheric electrodynamics during both disturbed and quiet time conditions. Finally, we developed a new empirical model of SAPS potentials parameterized by MLAT/MLT location and Asy-H index. This model can be easily used as a space weather prediction tool and would also be useful for validating the predictions of numerical simulations.

Acknowledgments
The authors thank the National Science Foundation (NSF) for support under grants AGS-1822056, AGS-1341918, AGS-1243070, and AGS-1150789. Asy-H index was obtained from the World Data Center in Kyoto. The majority of analysis and visualization were completed with the help of free, open source software tools such as Pandas (McKinney, 2010), DaViTpy (de Larquier et al., 2013), and matplotlib (Hunter, 2007). K. O. is grateful for being selected as the 2017–2018 Fulbright Arctic Chair, and his sabbatical at Virginia Tech was sponsored by the U.S. Norway Fulbright Foundation for Educational Exchange. K. O. also acknowledges support from the Research Council of Norway under contract 223252. S. G. S. acknowledges NSF for support under grant AGS-1341925.

References

Anderson, P. C., Carpenter, D. L., Tsuruda, K., Mukai, T., & Rich, F. J. (2001). Multisatellite observations of rapid subauroral ion drifts (SAID). *Journal of Geophysical Research*, *106*(A12), 29,585–29,599. https://doi.org/10.1029/2001JA000128

Anderson, P. C., Hanson, W. B., Heelis, R. A., Craven, J. D., Baker, D. N., & Frank, L. A. (1993). A proposed production model of rapid subauroral ion drifts and their relationship to substorm evolution. *Journal of Geophysical Research*, *98*(A4), 6069–6078. https://doi.org/10.1029/92JA01975

Banks, P. M., & Yasuhara, F. (1978). Electric fields and conductivity in the nighttime E-region: A new magnetosphere-ionosphere-atmosphere coupling effect. *Geophysical Research Letters*, *5*(12), 1047–1050. https://doi.org/10.1029/GL005i012p01047

Chisham, G., Lester, M., Milan, S. E., Freeman, M. P., Bristow, W. A., Grocott, A., et al. (2007). A decade of the Super Dual Auroral Radar Network (SuperDARN): Scientific achievements, new techniques and future directions. *Surveys in Geophysics*, *28*(1), 33–109. https://doi.org/10.1007/s10712-007-9017-8

Clausen, L. B. N., Baker, J. B. H., Ruohoniemi, J. M., Greenwald, R. A., Thomas, E. G., Shepherd, S. G., et al. (2012). Large-scale observations of a subauroral polarization stream by midlatitude SuperDARN radars: Instantaneous longitudinal velocity variations. *Journal of Geophysical Research*, *117*, A05306. https://doi.org/10.1029/2011JA017232

de Larquier, S., Ribeiro, A., Frissell, N. A., Spaleta, J., Kunduri, B., Thomas, E. G., et al. (2013). A new open-source Python-based Space Weather data access, visualization, and analysis toolkit (AGU Fall Meeting Abstracts, Abstract id. IN51B-1545). San Francisco, CA.

de Larquier, S., Ruohoniemi, J. M., Baker, J. B. H., Ravindran Varrier, N., & Lester, M. (2011). First observations of the midlatitude evening anomaly using super dual auroral radar network (SuperDARN) radars. *Journal of Geophysical Research*, *116*, A10321. https://doi.org/10.1029/2011JA016787

Ebihara, Y., Nishitani, N., Kikuchi, T., Ogawa, T., Hosokawa, K., Fok, M.-C., & Thomsen, M. F. (2009). Dynamical property of storm time subauroral rapid flows as a manifestation of complex structures of the plasma pressure in the inner magnetosphere. *Journal of Geophysical Research*, *114*, A01306. https://doi.org/10.1029/2008JA013614

Erickson, P. J., Beroz, F., & Miskin, M. Z. (2011). Statistical characterization of the American sector subauroral polarization stream using incoherent scatter radar. *Journal of Geophysical Research*, *116*, A00J21. https://doi.org/10.1029/2010JA015738

Foster, J. C., Banks, P. M., & Doupnik, J. R. (1982). Electrostatic potential in the auroral ionosphere derived from Chatanika radar observations. *Journal of Geophysical Research*, *87*(A9), 7513–7524. https://doi.org/10.1029/JA087iA09p07513

Foster, J. C., & Burke, W. J. (2002). SAPS: A new categorization for sub-auroral electric fields. *Eos, Transactions American Geophysical Union*, *83*(36), 393–394. https://doi.org/10.1029/2002EO000289

Foster, J., Rideout, W., Sandel, B., Forrester, W., & Rich, F. (2007). On the relationship of saps to storm-enhanced density. *Journal of Atmospheric and Solar-Terrestrial Physics*, *69*(3), 303–313. https://doi.org/10.1016/j.jastp.2006.07.021

Foster, J. C., & Vo, H. B. (2002). Average characteristics and activity dependence of the subauroral polarization stream. *Journal of Geophysical Research*, *107*(A12), 1475. https://doi.org/10.1029/2002JA009409

Freeman, M. P., Southwood, D. J., Lester, M., Yeoman, T. K., & Reeves, G. D. (1992). Substorm-associated radar auroral surges. *Journal of Geophysical Research*, *97*, 12,173–12,185. https://doi.org/10.1029/92JA00697

Gallardo-Lacourt, B., Nishimura, Y., Lyons, L. R., Mishin, E. V., Ruohoniemi, J. M., Donovan, E. F., et al. (2017). Influence of auroral streamers on rapid evolution of ionospheric saps flows. *Journal of Geophysical Research: Space Physics*, *122*, 12,406–12,420. https://doi.org/10.1002/2017JA024198

Galperin, Y., Ponomarev, V., & Zosimova, A. (1974). Plasma convection in the polar ionosphere. *Annales Geophysical Research*, *30*, 1–7.

Goldstein, J., Burch, J. L., & Sandel, B. R. (2005). Magnetospheric model of subauroral polarization stream. *Journal of Geophysical Research*, *110*, A09222. https://doi.org/10.1029/2005JA011135

Goldstein, J., Sandel, B. R., Hairston, M. R., & Reiff, P. H. (2003). Control of plasmaspheric dynamics by both convection and sub-auroral polarization stream. *Geophysical Research Letters*, *30*(24), 2243. https://doi.org/10.1029/2003GL018390

Greenwald, R., Baker, K., Dudeney, J., Pinnock, M., Jones, T., Thomas, E., et al. (1995). DARN/SuperDARN. *Space Science Reviews*, *71*(1), 761–796. https://doi.org/10.1007/BF00751350

Greenwald, R. A., Baker, K. B., Hutchins, R. A., & Hanuise, C. (1985). An HF phased-array radar for studying small-scale structure in the high-latitude ionosphere. *Radio Science*, *20*(1), 63–79. https://doi.org/10.1029/RS020i001p00063

Gussenhoven, M. S., Hardy, D. A., & Heinemann, N. (1987). The equatorward boundary of auroral ion precipitation. *Journal of Geophysical Research*, *92*(A4), 3273–3283. https://doi.org/10.1029/JA092iA04p03273

He, F., Zhang, X., Wang, W., & Chen, B. (2016). Double-peak subauroral ion drifts (DSAIDS). *Geophysical Research Letters*, *43*, 5554–5562. https://doi.org/10.1002/2016GL069133

He, F., Zhang, X., Wang, W., Liu, L., Ren, Z., Yue, X., et al. (2018). Large-scale structure of subauroral polarization streams during the main phase of a severe geomagnetic storm. *Journal of Geophysical Research: Space Physics*, *123*, 2964–2973. https://doi.org/10.1002/2018JA025234

He, F., Zhang, X., Wang, W., & Wan, W. (2017). Different evolution patterns of subauroral polarization streams (SAPS) during intense storms and quiet time substorms. *Geophysical Research Letters*, *44*, 10,796–10,804. https://doi.org/10.1002/2017GL075449

Heinemann, N. C., Gussenhoven, M. S., Hardy, D. A., Rich, F. J., & Yeh, H.-C. (1989). Electron/ion precipitation differences in relation to region 2 field-aligned currents. *Journal of Geophysical Research*, *94*(A10), 13,593–13,600. https://doi.org/10.1029/JA094iA10p13593

Hunter, J. D. (2007). Matplotlib: A 2D graphics environment. *Computing in Science and Engineering*, *9*(3), 90–95. https://doi.org/10.1109/MCSE.2007.55

Iyemori, T., Araki, T., Kamei, T., & Takeda, M. (1992). Mid-latitude geomagnetic indices ASY and SYM (provisional) no. 1, 1989 (Internal Report of Data Analysis Center for Geomagnetism and Space Magnetism), Kyoto University Kyoto.

Iyemori, T., & Rao, D. (1996). Decay of the DST field of geomagnetic disturbance after substorm onset and its implication to storm-substorm relation. *Annales Geophysicae*, *14*, 608–618.

Karlsson, T., Marklund, G. T., Blomberg, L. G., & Mälkki, A. (1998). Subauroral electric fields observed by the Freja satellite: A statistical study. *Journal of Geophysical Research*, *103*(A3), 4327–4341. https://doi.org/10.1029/97JA00333

Kataoka, R., Nishitani, N., Ebihara, Y., Hosokawa, K., Ogawa, T., Kikuchi, T., & Miyoshi, Y. (2007). Dynamic variations of a convection flow reversal in the subauroral postmidnight sector as seen by the SuperDARN Hokkaido HF radar. *Geophysical Research Letters*, *34*, L21105. https://doi.org/10.1029/2007GL031552

Kepko, L., McPherron, R. L., Amm, O., Apatenkov, S., Baumjohann, W., Birn, J., et al. (2015). Substorm current wedge revisited. *Space Science Reviews*, *190*(1), 1–46. https://doi.org/10.1007/s11214-014-0124-9

Kim, H., Cai, X., Clauer, C. R., Kunduri, B. S. R., Matzka, J., Stolle, C., & Weimer, D. R. (2013). Geomagnetic response to solar wind dynamic pressure impulse events at high-latitude conjugate points. *Journal of Geophysical Research: Space Physics*, *118*, 6055–6071. https://doi.org/10.1002/jgra.50555

Kunduri, B. S. R., Baker, J. B. H., Ruohoniemi, J. M., Clausen, L. B. N., Grocott, A., Thomas, E. G., et al. (2012). An examination of inter-hemispheric conjugacy in a subauroral polarization stream. *Journal of Geophysical Research*, *117*, A08225. https://doi.org/10.1029/2012JA017784

Kunduri, B. S. R., Baker, J. B. H., Ruohoniemi, J. M., Thomas, E. G., Shepherd, S. G., & Sterne, K. T. (2017). Statistical characterization of the large-scale structure of the sub-auroral polarization stream. *Journal of Geophysical Research: Space Physics*, *122*, 6035–6048. https://doi.org/10.1002/2017JA024131

Lejosne, S., Kunduri, B. S. R., Mozer, F. S., & Turner, D. L. (2018). Energetic electron injections deep into the inner magnetosphere: A result of the subauroral polarization stream (SAPS) potential drop. *Geophysical Research Letters*, *45*, 3811–3819. https://doi.org/10.1029/2018GL077969

Lejosne, S., & Mozer, F. S. (2017). Subauroral polarization streams (SAPS) duration as determined from Van Allen Probe successive electric drift measurements. *Geophysical Research Letters*, *44*, 9134–9141. https://doi.org/10.1002/2017GL074985

Liemohn, M. W., Kozyra, J. U., Thomsen, M. F., Roeder, J. L., Lu, G., Borovsky, J. E., & Cayton, T. E. (2001). Dominant role of the asymmetric ring current in producing the stormtime Dst*. *Journal of Geophysical Research*, *106*, 10,883–10,904. https://doi.org/10.1029/2000JA000326

Lyons, L. R., Nishimura, Y., Gallardo-Lacourt, B., Nicolls, M. J., Chen, S., Hampton, D. L., et al. (2015). Azimuthal flow bursts in the inner plasma sheet and possible connection with SAPS and plasma sheet earthward flow bursts. *Journal of Geophysical Research: Space Physics*, *120*, 5009–5021. https://doi.org/10.1002/2015JA021023

Maimaiti, M., Ruohoniemi, J. M., Baker, J. B. H., & Ribeiro, A. J. (2018). Statistical study of nightside quiet time mid-latitude ionospheric convection. *Journal of Geophysical Research: Space Physics*, *123*, 2228–2240. https://doi.org/10.1002/2017JA024903

McKinney, W. (2010). Data structures for statistical computing in python. In S. van der Walt & J. Millman (Eds.), *Proceedings of the 9th Python in Science Conference* (pp. 51–56). Austin, TX.

Mishin, E. V. (2013). Interaction of substorm injections with the subauroral geospace: 1. Multispacecraft observations of SAID. *Journal of Geophysical Research: Space Physics*, *118*, 5782–5796. https://doi.org/10.1002/jgra.50548

Mishin, E. V. (2016). SAPS onset timing during substorms and the westward traveling surge. *Geophysical Research Letters*, *43*, 6687–6693. https://doi.org/10.1002/2016GL069693

Mishin, E. V., Burke, W. J., Huang, C. Y., & Rich, F. J. (2003). Electromagnetic wave structures within subauroral polarization streams. *Journal of Geophysical Research*, *108*(A8), 1309. https://doi.org/10.1029/2002JA009793

Mishin, E., Nishimura, Y., & Foster, J. (2017). SAPS/SAID revisited: A causal relation to the substorm current wedge. *Journal of Geophysical Research: Space Physics*, *122*, 8516–8535. https://doi.org/10.1002/2017JA024263

Nagano, H., Nishitani, N., & Hori, T. (2015). Occurrence characteristics and lowest speed limit of subauroral polarization stream (SAPS) observed by the SuperDARN Hokkaido east radar. *Earth, Planets and Space*, *67*(1), 126. https://doi.org/10.1186/s40623-015-0299-7

Oksavik, K., Greenwald, R. A., Ruohoniemi, J. M., Hairston, M. R., Paxton, L. J., Baker, J. B. H., et al. (2006). First observations of the temporal/spatial variation of the sub-auroral polarization stream from the SuperDARN wallops HF radar. *Geophysical Research Letters*, *33*, L12104. https://doi.org/10.1029/2006GL026256

Parkinson, M. L., Pinnock, M., Ye, H., Hairston, M. R., Devlin, J. C., Dyson, P. L., et al. (2003). On the lifetime and extent of an auroral westward flow channel (AWFC) observed during a magnetospheric substorm. *Annales Geophysicae*, *21*(4), 893–913. https://doi.org/10.5194/angeo-21-893-2003

Prikryl, P., Ghoddousi-Fard, R., Kunduri, B. S. R., Thomas, E. G., Coster, A. J., Jayachandran, P. T., et al. (2013). GPS phase scintillation and proxy index at high latitudes during a moderate geomagnetic storm. *Annales Geophysicae*, *31*(5), 805–816. https://doi.org/10.5194/angeo-31-805-2013

Ribeiro, A. J., Ruohoniemi, J. M., Baker, J. B. H., Clausen, L. B. N., Greenwald, R. A., & Lester, M. (2012). A survey of plasma irregularities as seen by the midlatitude blackstone SuperDARN radar. *Journal of Geophysical Research*, *117*, A02311. https://doi.org/10.1029/2011JA017207

Ruohoniemi, J. M., & Baker, K. B. (1998). Large-scale imaging of high-latitude convection with super dual auroral radar network HF radar observations. *Journal of Geophysical Research*, *103*(A9), 20,797–20,811. https://doi.org/10.1029/98JA01288

Ruohoniemi, J. M., Greenwald, R. A., Baker, K. B., Villain, J.-P., Hanuise, C., & Kelly, J. (1989). Mapping high-latitude plasma convection with coherent HF radars. *Journal of Geophysical Research*, *94*(A10), 13,463–13,477. https://doi.org/10.1029/JA094iA10p13463

Ruohoniemi, J. M., Greenwald, R. A., Baker, K. B., Villain, J. P., & McCready, M. A. (1987). Drift motions of small-scale irregularities in the high-latitude F region: An experimental comparison with plasma drift motions. *Journal of Geophysical Research*, *92*(A5), 4553–4564. https://doi.org/10.1029/JA092iA05p04553

Schunk, R. W., Banks, P. M., & Raitt, W. J. (1976). Effects of electric fields and other processes upon the nighttime high-latitude F layer. *Journal of Geophysical Research*, *81*(19), 3271–3282. https://doi.org/10.1029/JA081i019p03271

Shi, X., Ruohoniemi, J. M., Baker, J. B. H., Lin, D., Bland, E. C., Hartinger, M. D., & Scales, W. A. (2018). Survey of ionospheric Pc3-5 ULF wave signatures in SuperDARN high time resolution data. *Journal of Geophysical Research: Space Physics*, *123*, 4215–4231. https://doi.org/10.1029/2017JA025033

Spiro, R. W., Heelis, R. A., & Hanson, W. B. (1979). Rapid subauroral ion drifts observed by Atmosphere Explorer C. *Geophysical Research Letters*, *6*(8), 657–660. https://doi.org/10.1029/GL006i008p00657

Thébault, E., Finlay, C. C., Beggan, C. D., Alken, P., Aubert, J., Barrois, O., et al. (2015). International geomagnetic reference field: The 12th generation. *Earth, Planets and Space*, *67*(1), 1–19. https://doi.org/10.1186/s40623-015-0228-9

Toffoletto, F., Sazykin, S., Spiro, R., & Wolf, R. (2003). Inner magnetospheric modeling with the Rice Convection Model. *Space Science Reviews*, *107*(1), 175–196. https://doi.org/10.1023/A:1025532008047

Tsyganenko, N. A. (2002a). A model of the near magnetosphere with a dawn-dusk asymmetry 1. Mathematical structure. *Journal of Geophysical Research*, *107*(A8), 1179. https://doi.org/10.1029/2001JA000219

Tsyganenko, N. A. (2002b). A model of the near magnetosphere with a dawn-dusk asymmetry 2. Parameterization and fitting to observations. *Journal of Geophysical Research*, *107*(A8), 1176. https://doi.org/10.1029/2001JA000220

Zou, S., Moldwin, M. B., Ridley, A. J., Nicolls, M. J., Coster, A. J., Thomas, E. G., & Ruohoniemi, J. M. (2014). On the generation/decay of the storm-enhanced density plumes: Role of the convection flow and field-aligned ion flow. *Journal of Geophysical Research: Space Physics*, *119*, 8543–8559. https://doi.org/10.1002/2014JA020408